

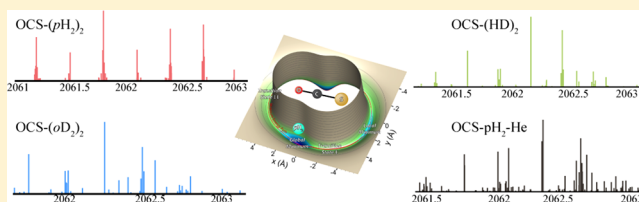
Theoretical Study of Infrared Spectra of OCS-(*p*H₂)₂, OCS-(*o*D₂)₂, OCS-(HD)₂, and Mixed OCS-*p*H₂-He Trimers

Jing-Min Liu, Xiao-Long Zhang, Yu Zhai, and Hui Li*

Laboratory of Theoretical and Computational Chemistry, Institute of Theoretical Chemistry, Jilin University, 2519 Jiefang Road, Changchun 130023, P. R. China

Supporting Information

ABSTRACT: The calculated rovibrational energy levels and infrared spectra for OCS-(*p*H₂)₂, OCS-(*o*D₂)₂, OCS-(HD)₂ and mixed OCS-*p*H₂-He trimers are obtained by performing the exact basis-set calculations for the first time based on the newly developed potential energy surfaces (*J. Chem. Phys.* 2017, 147, 044313). The “adiabatic-hindered-rotor” (AHR) method is used for reduced-dimension treatment of the hydrogen rotation. The predicted band origin shifts and the infrared spectra are in good agreement with the available experimental values: for the band origin shifts and infrared transitions, the root-mean-square(rms) deviations are smaller than 0.044 and 0.002 cm⁻¹, respectively. We extend the assignments to the unrecorded infrared transitions for OCS-(*p*H₂)₂ and OCS-(HD)₂ complexes and identify the infrared spectra for OCS-(*o*D₂)₂ and OCS-*p*H₂-He for the first time. Three-dimensional density distributions for the ground states of OCS-(*p*H₂)₂, OCS-*p*H₂-He, and OCS-(He)₂ show that the *p*H₂ molecules are localized in their corresponding global minimum regions, while the pronounced locations of the He atoms are missing in OCS-*p*H₂-He and OCS-(He)₂ with forming incomplete circles around the OCS axis. A clear tunneling splitting is observed for the torsional motion of the two hydrogen molecules (*p*H₂, HD, or *o*D₂) on a ring about the OCS molecular axis, whereas no tunneling splitting is found in OCS-*p*H₂-He or OCS-(He)₂ due to a much lower torsional barrier.



INTRODUCTION

High-resolution infrared and microwave studies of a chromophore molecule embedded in hydrogen clusters have been extensively explored during the past decades because they provide a new way to probe the microscopic molecular superfluidity.^{1–27} Among the chromophore molecules, OCS was the most widely used probe for experimental studies in doped hydrogen clusters coated with helium droplets or in bare hydrogen clusters.^{10–15,17–27}

The first breakthrough belonged to Grebenev et al.¹⁰ They observed the infrared spectra of OCS-(*p*H₂)_N (*N* = 14–16) and OCS-(*o*D₂)_N (*N* = 15–17) embedded in ⁴He and in mixed ⁴He/³He droplets and found that the Q-branch of OCS-(*p*H₂)_N disappeared while it always existed in OCS-(*o*D₂)_N. The disappearance of Q-branch of OCS-(*p*H₂)_N was attributed to the moment of inertia about the OCS axis decreasing to zero when temperature reduced from 0.38 to 0.15 K, which was considered to be the first experimental evidence for *p*H₂ superfluidity. In their later research, they found that the Q-branch was also absent for OCS-(*p*H₂)_N (*N* = 5, 6, and 12), which was intrinsically related to the permutation of *p*H₂ around dopant OCS.^{11–14} However, the structures they proposed were not consistent with those calculated without helium droplets.¹⁶ Therefore, helium droplets may not only act as thermostats. The structural and spectral properties for pure OCS-(*p*H₂)_N still need further studies.

Tang and McKellar conducted the first infrared spectroscopic (IR) study of OCS with pure hydrogen. They observed the high resolution infrared spectra for OCS-(H₂)_N clusters with

N up to 7 following their initial investigation of OCS-H₂ dimer.^{15,17} There was no Q-branch for doped *p*H₂ clusters, as they recorded, but it existed in the other species of OCS-(hydrogen)_N complexes. However, the disappearance of the Q-branch can not be directly related to the superfluidity of *p*H₂, because the absence of the Q-branch also happened for *N* = 1 where there was no bosonic exchange. They attributed the phenomenon to symmetric rotor structures, low effective rotational temperature (0.15–0.6 K) and the nuclear spin statistics. In addition to the infrared studies, the microwave spectra were investigated by Yu et al., Michaud et al., and Raston et al. for all the five species of OCS-H₂ complexes in size range of *N* = 1–7.^{18–22} Due to the experimental limits, the spectroscopic assignments were stopped at *N* = 7. In order to identify larger clusters and to gain insight into the structural nature of OCS-(H₂)_N, theoretical simulations are required to provide more detailed information about this subject.

Until now, three groups have simulated the OCS-(H₂)_N clusters.^{23–27} Kwon and Whaley performed the PIMC simulation for OCS-(*p*H₂)_N (*N* = 17) and obtained the anisotropic superfluid response.²³ However, they have not provided the infrared spectra or band origin shift because the PES they used was with OCS fixed at its experimental equilibrium bond length. Using the same potential energy surface, Piccarreta and

Received: December 26, 2017

Revised: March 1, 2018

Published: March 1, 2018



Gianturco studied clusters with N up to 30 for $\text{OCS}-(p\text{H}_2)_N$, where the structural features of a varying number of $p\text{H}_2$ molecules bound to OCS were examined. Paesani and co-workers presented the calculated structures and the solvent vibrational shifts for $\text{OCS}-(p\text{H}_2)_N$ ($N = 1\sim 17$) clusters based on their PESs (V_{MP4}) which were computed using the fourth-order Möller-Plesset (MP4) perturbation theory with including Q_1 (C-O stretching) normal mode coordinate.¹⁶ However, the predicted band origin shift of $\text{OCS}-o\text{H}_2$ based on their PESs was two times larger than the corresponding experiment value, which should be attributed to the quality of their PESs.²⁸ Recently, we presented a highly precise PES which explicitly incorporated both Q_1 and Q_3 (C-S stretching) normal mode coordinates with a high-level calculation method, and the resulted spectral data were in excellent agreement with the corresponding experimental values. Furthermore, instead of a simple spherical averaged approximation, Li et al. developed a new effective reduced-dimension treatment technique which enables to treat H_2 as a point-like particle.²⁹ That makes it possible to calculate the exact infrared spectra with particle (e.g., $p\text{H}_2$) numbers up to two or even three. In this work, we extend our assignments of the dimers' infrared spectra to the cases of $\text{OCS}-(p\text{H}_2)_2$, $\text{OCS}-(o\text{D}_2)_2$, and $\text{OCS}-(\text{HD})_2$ (these three are referred to as $\text{OCS}-(\text{hydrogen})_2$) to fully understand the trimers spectroscopic properties and to perform benchmark tests for the larger clusters. Since a thorough understanding of small $\text{OCS}-\text{H}_2$ complex promotes research on larger systems. In addition to the pure clusters ($\text{OCS}-(\text{hydrogen})_2$), the mixed cluster of $\text{OCS}-p\text{H}_2\text{-He}$ is also studied, which was motivated by the fact that the spectroscopic features of OCS doped in H_2 clusters are quite different with those coated by helium droplets. Besides, this work will provide a guidance to assign the infrared transitions with weaker intensities at a relatively low temperature (0.6 or 0.2 K).

METHODOLOGY

Geometry and Reduced-Dimension Treatment. To describe the full dimensional intra- and intermolecular interactions of $\text{OCS}-(\text{hydrogen})_2$ system, 15-dimensional ($3 \times 7 - 6 = 15$) coordinates are required. It still needs nine intermolecular degrees of freedom even if we treat OCS and the two H_2 as rigid molecules. The geometry of the nine-dimensional complex can be naturally described using Jacobi coordinates as shown on the left panel of Figure 1, where q'_1 and q'_2 are the distances

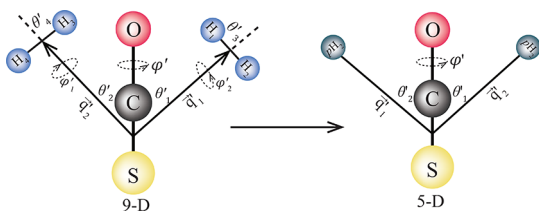


Figure 1. Jacobi coordinates for the $\text{OCS}-(\text{H}_2)_2$ complex: left panel shows the nine-dimensional intermolecular coordinates and the right panel displays the five-dimensional intermolecular coordinates with the approximation of AHR.

from the center mass of OCS to the center mass of H_2 , θ'_1 and θ'_2 are the angles between q'_1 and q'_2 and the vectors pointing from atom S to atom O, θ'_3 and θ'_4 are the angles between q'_1 and q'_2 and the vectors pointing from H_2 to H_1 and from H_4 to H_3 , ϕ'_1 and ϕ'_2 are the azimuthal angles for rotations of $\text{H}_1\text{-H}_2$ and $\text{H}_3\text{-H}_4$ about vectors of q'_1 and q'_2 , and ϕ is the dihedral angle between two planes between vectors q'_1 , q'_2 and the axis of

OCS molecular. It remains infeasible to solve the exact quantum nine-dimensional intermolecular Schrödinger equation. Thus, a reduced-dimension treatment is necessary.

Usually, it is considered a good approximation to treat $p\text{H}_2$ as a spherical particle because the isolated ground-state ($J = 0$) H_2 molecular is precisely spherically symmetric and the spacing energy to its first excited level ($J = 2$) is relatively large (354.375 cm^{-1}). However, for H_2 -molecule complex, a simple spherical average over the relative orientations of H_2 moiety cannot provide an accurate description of $p\text{H}_2$ since it is not truly spherical symmetry in this kind of interactions.²⁹ Here, a much better reduced-dimension approximation named “Adiabatic-hindered-rotor” is used. By performing the Born–Oppenheimer-type separation of the fast rotational motion of $p\text{H}_2$ from the other degrees of freedom, Li, Roy and Le Roy got the effective spherical descriptions of $p\text{H}_2$ in $p\text{H}_2$ -{linear} interactions which were an order of magnitude better than those obtained by a simple spherical averaged approximation.²⁹ Indeed, this technique has been used in $\text{CO}_2-(p\text{H}_2)_2$,³⁰ $\text{CO}-(p\text{H}_2)_2$,³¹ $\text{CO}-(o\text{D}_2)_2$,³¹ and $\text{CO}-p\text{H}_2\text{-He}$ ³¹ trimers and in $\text{N}_2\text{O}-p\text{H}_2$ and $\text{H}_2\text{O}-p\text{H}_2$ ^{33,34} dimers. The good results validated the AHR method. Therefore, the AHR approximation is selected here to yield the two-dimensional PES of $p\text{H}_2\text{-OCS}$ based on our recently vibrationally averaged $4\text{D}-V_{\text{MLR}}$ PES.²⁸ A contour plot of the AHR averaged potential is shown in Figure 2. The global minimum locates at

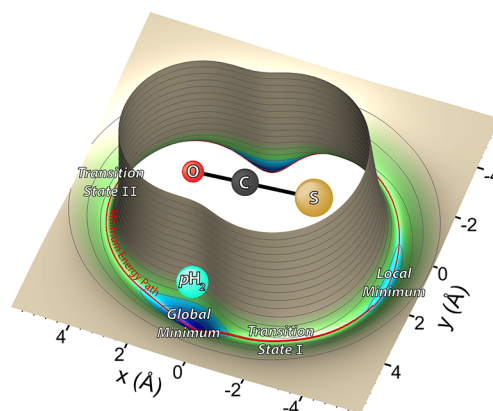


Figure 2. Contour plot of reduced-dimensional adiabatic-hindered-rotor averaged $2\text{d}-V_{\text{MLR}}$ PES for $\text{OCS}(v_1=0)-p\text{H}_2$ in cylindrical coordinates with $x = R \cos \theta$ and $y = R \sin \theta$.

$R = 3.377\text{ Å}$ and $\theta = 73.7^\circ$ with a well depth of 134.890 cm^{-1} . Two transition states are also found in Figure 2. The transition state I corresponding to -61.982 cm^{-1} situates at $R = 4.291\text{ Å}$ and $\theta = 125.8^\circ$ and the transition state II which links the two global minima due to the symmetry locates at $R = 4.937\text{ Å}$ and $\theta = 0.0^\circ$ having a interaction of -63.926 cm^{-1} . The local minimum occurs at $R = 4.514\text{ Å}$ and $\theta = 180.0^\circ$ with a well depth of 88.446 cm^{-1} . Thus, the relatively good reduced-dimension treatment of the $\text{OCS}-(p\text{H}_2)_2$ trimer would be obtained by the AHR approximation which is shown in the right panel of Figure 1. The same treatments are also applied for the other three trimers of $\text{OCS}-(o\text{D}_2)_2$, $\text{OCS}-(\text{HD})_2$ and $\text{OCS}-p\text{H}_2\text{-He}$.

Bound State Energy Levels and Intensities. In this work, the radial discrete variable representation (DVR) and parity-adapted angular finite basis representation (FBR) method followed by Wang and Carrington³⁵ is used to calculate the rovibrational levels whose fundamental ideas are presented by Mladenovic.³⁶ This approach is widely used in $\text{N}_2\text{O}-(\text{He})_2$, $\text{CO}-(\text{He})_2$, $\text{CO}_2-(\text{He})_2$, $\text{OCS}-(\text{He})_2$, $\text{CO}_2-(p\text{H}_2)_2$, and $\text{CO}-(p\text{H}_2)_2$

complexes.^{30,31,35,37–39} The excellent agreement with experiment values validates this method. Here, we will review this approach briefly, and the details can be found in ref 35.

The rovibrational Hamiltonian of the OCS-(H₂)₂ or OCS-H₂-He complex in the body-fixed frame has the form of (in a.u.):^{35,36,40,41}

$$\hat{H} = \hat{T}_{\text{str}} + \hat{T}_{\text{diag}} + \hat{T}_{\text{off}} + \hat{T}_{\text{Cor}} + \bar{V}(r_1, r_2, \theta_1, \theta_2, \varphi). \quad (1)$$

The stretching part (\hat{T}_{str}) is

$$\hat{T}_{\text{str}} = -\frac{1}{2m_1} \frac{\partial^2}{\partial r_1^2} - \frac{1}{2m_2} \frac{\partial^2}{\partial r_2^2}. \quad (2)$$

The diagonal (\hat{T}_{diag}) and off-diagonal (\hat{T}_{off}) of bend-rotation part and Coriolis part (\hat{T}_{Cor}) are

$$\begin{aligned} \hat{T}_{\text{diag}} = & -\left(\frac{1}{2m_1 r_1^2} + B_{\text{OCS}} \right) \\ & \times \left[\frac{\partial^2}{\partial \theta_1^2} + \cot \theta_1 \frac{\partial}{\partial \theta_1} - \frac{1}{\sin^2 \theta_1} (\hat{J}_z - \hat{l}_{2z})^2 \right] \\ & + \left(\frac{1}{2m_2 r_2^2} + B_{\text{OCS}} \right) \hat{l}_2^2 + B_{\text{OCS}} [\hat{J}^2 - 2(\hat{J}_z - \hat{l}_{2z})^2 - 2\hat{J}_z \hat{l}_{2z}] \end{aligned} \quad (3)$$

$$\hat{T}_{\text{off}} = B_{\text{OCS}} [\hat{l}_{2+} \hat{a}_1^- + \hat{l}_{2-} \hat{a}_1^+] \quad (4)$$

$$\hat{T}_{\text{Cor}} = -B_{\text{OCS}} [\hat{J}_- \hat{a}_1^+ + \hat{J}_+ \hat{a}_1^- + \hat{J}_- \hat{l}_{2+} + \hat{J}_+ \hat{l}_{2-}] \quad (5)$$

in which

$$\hat{J}_{\pm} = \hat{J}_x \pm i\hat{J}_y, \quad \hat{l}_{2\pm} = \hat{l}_{2x} \pm i\hat{l}_{2y} \quad (6)$$

$$\hat{a}_1^{\pm} = \pm \frac{\partial}{\partial \theta_1} - \cot \theta_1 (\hat{J}_z - \hat{l}_{2z}) \quad (7)$$

r_1 and r_2 are the lengths of Radau vectors which are presented in Figure 3. m_1 is the mass of H₂ molecule, m_2 is the mass of H₂

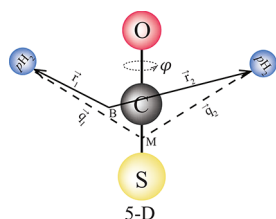


Figure 3. Radau coordinates which were used in the bound state calculations. M is the center of mass of OCS and B is the canonical point for Radau vectors of r_1 and r_2 which are linear combinations of Jacobi vectors of q_1 and q_2 , and r_0 is a vector along the axis of OCS. φ is the dihedral angle between $r_1 \times r_0$ and $r_2 \times r_0$, and θ_1 and θ_2 are angles between r_0 , r_1 , and r_2 , respectively.

molecule or He atom, and B_{OCS} is the inertial rotational constant of OCS. The operators \hat{J}_x , \hat{J}_y , and \hat{J}_z are the components of the total angular momentum operator \hat{J} in the body-fixed frame. The z axis of the body-fixed frame lies along the Jacobi radial vector r_0 , and its x axis is in the plane that contains the vector r_0 and a H₂ molecule or a He atom. $\bar{V}(r_1, r_2, \theta_1, \theta_2, \varphi)$ is the total potential as a sum of three pair potentials:

$$\begin{aligned} \bar{V}(r_1, r_2, \theta_1, \theta_2, \varphi) &= \bar{V}(q_1, q_2, \theta_1', \theta_2', r_{12}) \\ &= \bar{V}(q_1, \theta_1') + \bar{V}(q_2, \theta_2') + \bar{V}(r_{12}) \end{aligned} \quad (8)$$

where $\bar{V}(r_1, r_2, \theta_1, \theta_2, \varphi)$ and $\bar{V}(q_1, q_2, \theta_1', \theta_2', r_{12})$ are the total potentials in Radau and Jacobi coordinates, respectively. $\bar{V}(q_1, \theta_1')$ and $\bar{V}(q_2, \theta_2')$ are the potentials of OCS-hydrogen and OCS-hydrogen or OCS-He, and $\bar{V}(r_{12})$ is the potential of hydrogen-hydrogen or hydrogen-helium in Jacobi coordinates. The interactions of the OCS-hydrogen complex (OCS-*p*H₂, OCS-HD and OCS-*o*H₂) are achieved by the AHR average using dimer potentials taken from ref 28, while hydrogen-hydrogen potentials are obtained by a “spherical” average treatment of H₂ rotation with the dimer potential taken from ref 42, and OCS-He potentials are used from ref 43 for OCS-*p*H₂-He.^{42,43} The PES of H₂-He was calculated at the CCSD(T)/CBS level extrapolated from the aug-cc-pVXZ ($X = Q, 5$) basis sets with bond functions. The above Hamiltonian contains full vibration–rotation coupling.

A sinc discrete variable representation (DVR) grid^{44,45} is used for the radial degree of freedom, and the parity-adapted rovibrational basis functions are adopted for the angle part. Following our previous work,³⁰ the complete product basis function is

$$\begin{aligned} u_{l_1, l_2, m_2, K}^{J, M, P} &= \frac{1}{\sqrt{2(1 + \delta_{m_2, 0} \delta_{K, 0})}} [l_{l_1, l_2, m_2, K; J, M} \\ &+ (-1)^{J+P} l_{l_1, l_2, -m_2, -K; J, M}], \end{aligned} \quad (9)$$

where l_1 and l_2 are the rotational angular momentum quantum numbers of Radau vectors of r_1 and r_2 , respectively. $P = 0$ or 1 is the space-inversion parity, and M and K quantum numbers are the projections of the total angular momentum J on to the space-fixed and body-fixed frame, respectively. When $K > 0$, $P = 0$ and 1 correspond to even and odd parities, respectively. It is necessary to apply the constraint $m_2 \geq 0$ to get rid of redundant basis if $K = 0$. Note that the combination of $m_2 = K = 0$ and $(-1)^{J+P} = -1$ is not allowed. With the parity-adapted basis, we calculate the even and odd levels separately. The symmetry-adapted Lanczos algorithm^{46,47} is used to compute the states that are symmetric (A) and antisymmetric (B) with respect to exchange of the two *p*H₂, *o*D₂, and HD-HD in OCS-(*p*H₂)₂, OCS-(*o*D₂)₂, and OCS-(HD)₂ complexes while there is no exchange symmetry applying for OCS-*p*H₂-He.

In the computation of the rovibrational energy levels, the inertial rotational constants B_{OCS} required for these calculations are fixed at the experimental values of 0.202856741 and 0.201641526 cm^{−1} for the ground ($v_1 = 0$) and excited ($v_1 = 1$) states, respectively.⁴⁸ A 40-point sine DVR grid range from 3.0 to 30.0 bohr is used for the radial r_1 and r_2 stretching coordinates. $l_{\text{max}} = m_{\text{max}} = 25$ is used for the angular basis. Thirty Gauss-Legendre quadrature points are used to integrate over θ_1 or θ_2 , and 64 equally spaced points in the range of $[0, 2\pi]$ are used for the integration over φ . It has been proven that using the potential ceiling value would reduce the spectral range and accelerate the convergence of Lanczos calculations.⁴⁹ In this work, we use a ceiling of 1000 cm^{−1} and have confirmed that low-lying energy levels change by less than 0.001 cm^{−1} when the ceiling raising to 10 000 cm^{−1}.

The transition intensities can be written as

$$S_{i' i} = 3 \sum_{M, M'} |\langle \Psi_{i'} | \mu_0^{\text{SF}} | \Psi_i \rangle|^2 \quad (10)$$

where μ_0^{SF} is the space-fixed Z -component of dipole moment operator and Ψ_i is the rovibrational wave function. μ_0^{SF} is first transformed from monomer-fixed (MF) to body-fixed (BF) and

then to space-fixed (SF) frame via two steps of rotational coordinates transformations. μ_0^{SF} can be written as a product of molecular dipole moments of OCS with two rotational functions. More details are given in our previous work.³⁰ The relative infrared intensity for a transition from a lower state i' to an upper state i is

$$I_{ii'} \propto e^{-E_{i'}/k_B T} \times S_{ii'} \quad (11)$$

by assuming that radiation is absorbed by molecules at thermal equilibrium at temperature T . $E_{i'}$ is the energy of lower state i' relative to the lowest bound state.

RESULTS AND DISCUSSION

Features of the Five-Dimensional Potential Energy Surface. Figure 4 displays the contour lines of our vibrationally

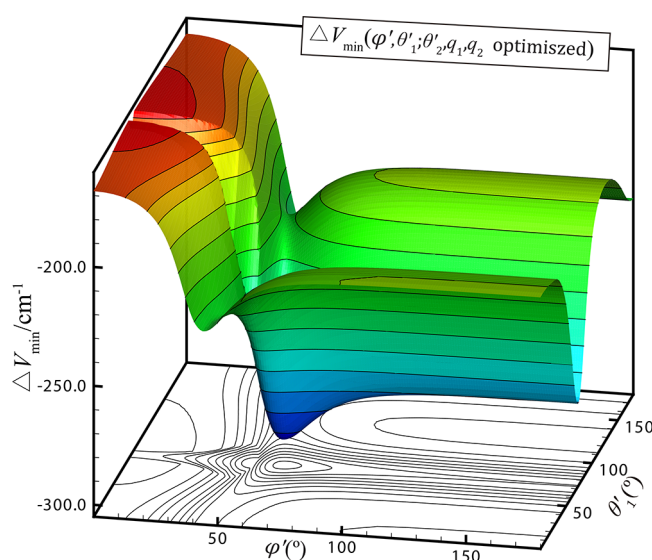


Figure 4. Minimum energy on our vibrationally averaged SD PES for $\text{OCS}(v_1=0)\text{-(pH}_2)_2$ as a function of angles of φ' and θ'_1 with θ'_2 , q_1 , and q_2 optimized.

averaged five-dimensional V_{MLR} potential energy surface (PES) for $\text{OCS-(pH}_2)_2$ along φ' and θ'_1 coordinates where q_1 , q_2 , and θ'_2 are optimized. As Figure 4 shows, a global minimum with a well depth of 294.41 cm^{-1} occurs at $\theta'_1 = \theta'_2 = 73.1^\circ$, $q_1 = q_2 = 3.38 \text{ \AA}$, and $\varphi' = 61.6^\circ$ (or $\varphi' = 298.4^\circ$ by symmetry). Linking two identical global minima, saddle point I has a location of $\theta'_1 = \theta'_2 = 73.2^\circ$, $q_1 = q_2 = 3.37 \text{ \AA}$, and $\varphi' = 180.0^\circ$ corresponding to a coplanar geometry with an energy gap of 23.95 cm^{-1} relative to the global minimum. In addition, there still exists a coplanar saddle point (noted as saddle point II) situated at $\theta'_1 = 0.0^\circ$, $\theta'_2 = 73.3^\circ$, $q_1 = 6.76 \text{ \AA}$, $q_2 = 3.36 \text{ \AA}$, and $\varphi' = 0.0^\circ$ where one of the pH_2 is collinear with the OCS molecule and the other

locates nearly the global minima position with a considerable barrier of 126.24 cm^{-1} relative to the global minimum. Parameters of the various stationary configurations and energies are summarized in Table 1, where OCS-(hydrogen)_2 trimers are compared with $\text{OCS-pH}_2\text{-He}$, $\text{CO}_2\text{-(pH}_2)_2$, and OCS-(He)_2 complexes.

As shown in Table 1, the energies of global minimum, saddle point I, and saddle point II are similar to each other for the OCS-(hydrogen)_2 complexes with energy differences smaller than 5 cm^{-1} . Except saddle point II of $\text{OCS-pH}_2\text{-He}$ whose energy is similar to $\text{OCS-(pH}_2)_2$, the stationary point energies for $\text{OCS-(pH}_2)_2$ are about 100 cm^{-1} lower than those for $\text{OCS-pH}_2\text{-He}$ and are almost three times deeper than those for OCS-(He)_2 due to the stronger polarizability of pH_2 (5.414 au)⁵⁰ comparing to that of He (1.383 au).⁵¹ Moreover, for $\text{CO}_2\text{-(pH}_2)_2$, the energies of all of the stationary points are almost 40 cm^{-1} higher than those of $\text{OCS-(pH}_2)_2$ due to the stronger polarizability of OCS (33.726 au)⁵² comparing to that of CO_2 (17.51 au).⁵³

Figure 5 displays the minimum energy paths (MEPs) as a function of φ' for optimizing the remaining variables. As shown

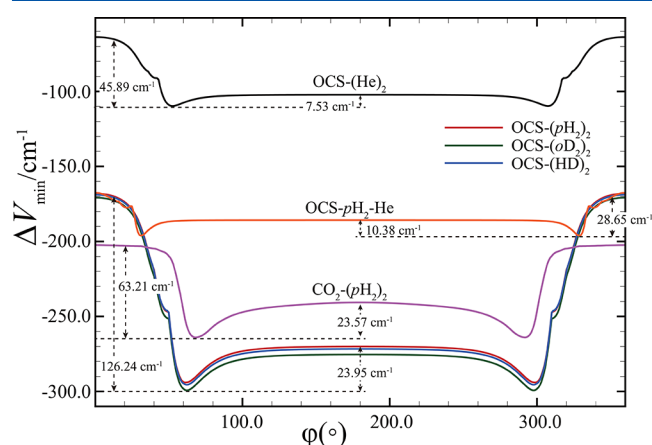


Figure 5. Minimum energy paths on our vibrationally averaged SD PESs for $\text{OCS}(v_1=0)\text{-(hydrogen)}_2$ and $\text{OCS}(v_1=0)\text{-pH}_2\text{-He}$ complexes as a function of φ' with θ'_1 , θ'_2 , q_1 , and q_2 optimized and compared with $\text{OCS}(v_1=0)\text{-(He)}_2$ and $\text{CO}_2(v_1=0)\text{-(pH}_2)_2$ trimers.

in Figure 5, the energy anisotropy with respect to the dihedral torsional motion of $\text{OCS-(pH}_2)_2$ are almost two, five, and three times larger than $\text{CO}_2\text{-(pH}_2)_2$, $\text{OCS-pH}_2\text{-He}$, and OCS-(He)_2 , respectively. The barrier between the two adjacent minima of $\text{OCS-(pH}_2)_2$ (23.95 cm^{-1}) is almost the same as $\text{CO}_2\text{-(pH}_2)_2$ (23.57 cm^{-1}) but is 13.57 cm^{-1} higher than $\text{OCS-pH}_2\text{-He}$ and three times higher than that for OCS-(He)_2 (7.53 cm^{-1}). The differences in barrier height may arise from the different well depths of $\text{pH}_2\text{-pH}_2$ (24.71 cm^{-1}), $\text{pH}_2\text{-He}$ (10.39 cm^{-1}), and He-He (7.65 cm^{-1}).

Table 1. Properties of Stationary Points of the $\text{OCS}(v_1=0)\text{-(Hydrogen)}_2$ and $\text{OCS}(v_1=0)\text{-pH}_2\text{-He}$ Complexes and Compared with $\text{OCS}(v_1=0)\text{-(He)}_2$ and $\text{CO}_2(v_1=0)\text{-(pH}_2)_2$ Trimers^a

	global minimum	saddle point I	saddle point II
$\text{OCS-(pH}_2)_2$	{3.38, 3.38, 73.1, 73.1, 61.6, -294.407}	{3.37, 3.37, 73.2, 73.2, 180.0, -270.461}	{6.76, 3.36, 0.0, 73.3, 0.0, -168.163}
$\text{OCS-(oD}_2)_2$	{3.36, 3.36, 73.0, 73.0, 62.0, -299.370}	{3.36, 3.36, 73.0, 73.0, 180.0, -275.438}	{3.34, 6.74, 73.3, 0.0, 0.0, -170.826}
OCS-(HD)_2	{3.36, 3.36, 73.9, 73.9, 62.0, -295.701}	{3.36, 3.36, 73.9, 73.9, 180.0, -271.770}	{3.35, 6.75, 75.1, 0.0, 0.0, -168.891}
$\text{OCS-pH}_2\text{-He}$	{3.38, 3.35, 73.1, 70.1, 31.2, -196.329}	{3.38, 3.35, 73.1, 70.1, 180.0, -185.947}	{3.34, 5.08, 73.5, 0.0, 0.0, -167.680}
OCS-(He)_2 ³⁹	{3.35, 3.35, 70.1, 70.1, 52.5, -109.728}	{3.35, 3.35, 70.1, 70.1, 180.0, -102.202}	{6.20, 3.32, 0.0, 70.5, 0.0, -63.837}
$\text{CO}_2\text{-(pH}_2)_2$ ³⁰	{3.05, 3.05, 90.0, 90.0, 69.2, -265.630}	{3.14, 3.14, 90.0, 90.0, 180.0, -242.058}	{3.00, 4.00, 36.0, 92.0, 0.0, -202.420}

^aSD entries are given as $\{q_1[\text{\AA}], q_2[\text{\AA}], \theta'_1, \theta'_2, \varphi', \Delta V[\text{cm}^{-1}]\}$.

Table 2. Calculated Rovibrational Energy Levels (in cm^{-1}) with $J = 0, 1, 2$, and 3 for $\text{OCS}(\nu_1=0)$ -(Hydrogen) $_2$ Complexes and for $\text{OCS}(\nu_1=0)$ - $p\text{H}_2$ -He Trimer which Are Relative to the Corresponding Zero-Point Levels (-139.718 cm^{-1} for $\text{OCS}-(p\text{H}_2)_2$, -177.057 cm^{-1} for $\text{OCS}-(o\text{D}_2)_2$, -163.895 cm^{-1} for $\text{OCS}-(\text{HD})_2$, and -87.476 cm^{-1} for $\text{OCS}-p\text{H}_2$ -He)^a

OCS-($p\text{H}_2$) $_2$				OCS-($o\text{D}_2$) $_2$				OCS-(HD) $_2$				OCS- $p\text{H}_2$ -He	
(A,e)	(B,e)	(A,f)	(B,f)	(A,e)	(B,e)	(A,f)	(B,f)	(A,e)	(B,e)	(A,f)	(B,f)	e	f
$J = 0$													
0.000	25.249	25.316	0.081	0.000	23.936	23.936	0.001	0.000	25.143	25.146	0.008	0.000	0.538
(0;0 $_{00}$)			(1;0 $_{00}$)	(0;0 $_{00}$)			(1;0 $_{00}$)	(0;0 $_{00}$)			(1;0 $_{00}$)	(0;0 $_{00}$)	(1;0 $_{00}$)
5.182	31.473	35.355	9.023	7.423	35.408	35.969	9.131	6.390	35.123	36.328	8.794	2.641	5.829
(2;0 $_{00}$)			(3;0 $_{00}$)	(2;0 $_{00}$)			(3;0 $_{00}$)	(2;0 $_{00}$)			(3;0 $_{00}$)	(2;0 $_{00}$)	(3;0 $_{00}$)
14.359	32.814	35.867	20.952	11.915	37.821	37.916	15.686	12.484	37.963	38.375	17.256	8.211	10.240
(4;0 $_{00}$)			(5;0 $_{00}$)	(4;0 $_{00}$)			(5;0 $_{00}$)	(4;0 $_{00}$)			(5;0 $_{00}$)	(4;0 $_{00}$)	(5;0 $_{00}$)
26.789	34.492	39.517	27.171	20.253	38.775	41.778	25.500	22.932	38.832	42.803	28.101	9.515	12.779
$J = 1$													
0.610	0.385	0.305	0.528	0.349	0.248	0.247	0.348	0.420	0.282	0.275	0.412	0.418	0.273
(1;1 $_{10}$)	(0;1 $_{11}$)	(0;1 $_{01}$)	(0;1 $_{10}$)	(1;1 $_{10}$)	(0;1 $_{11}$)	(0;1 $_{01}$)	(0;1 $_{10}$)	(1;1 $_{10}$)	(0;1 $_{11}$)	(0;1 $_{01}$)	(0;1 $_{10}$)	(1;1 $_{10}$)	(0;1 $_{10}$)
9.513	0.525	0.604	5.664	9.429	0.339	0.340	7.709	9.161	0.402	0.409	6.745	0.806	0.381
(3;1 $_{10}$)	(1;1 $_{01}$)	(1;1 $_{11}$)	(2;1 $_{10}$)	(3;1 $_{10}$)	(1;1 $_{01}$)	(1;1 $_{11}$)	(2;1 $_{10}$)	(3;1 $_{10}$)	(1;1 $_{01}$)	(1;1 $_{11}$)	(2;1 $_{10}$)	(1;1 $_{01}$)	(0;1 $_{10}$)
21.432	5.720	5.498	14.848	15.987	7.785	7.695	12.216	17.624	6.815	6.683	12.853	0.929	0.945
(5;1 $_{10}$)	(2;1 $_{11}$)	(2;1 $_{01}$)	(4;1 $_{10}$)	(5;1 $_{10}$)	(2;1 $_{11}$)	(2;1 $_{01}$)	(4;1 $_{10}$)	(5;1 $_{10}$)	(2;1 $_{11}$)	(2;1 $_{01}$)	(4;1 $_{10}$)	(1;1 $_{10}$)	(1;1 $_{11}$)
25.615	9.331	9.548	25.549	24.174	9.390	9.478	20.553	25.413	9.077	9.205	23.293	3.058	2.916
	(3;1 $_{01}$)	(3;1 $_{11}$)			(3;1 $_{01}$)	(3;1 $_{11}$)			(3;1 $_{01}$)	(3;1 $_{11}$)		(2;1 $_{11}$)	(2;1 $_{01}$)
$J = 2$													
0.915	1.141	1.225	0.993	0.740	0.851	0.852	0.740	0.823	0.970	0.978	0.830	0.809	0.997
(0;2 $_{02}$)	(0;2 $_{11}$)	(0;2 $_{21}$)	(0;2 $_{12}$)	(0;2 $_{02}$)	(0;2 $_{11}$)	(0;2 $_{21}$)	(0;2 $_{12}$)	(0;2 $_{02}$)	(0;2 $_{11}$)	(0;2 $_{21}$)	(0;2 $_{12}$)	(0;2 $_{02}$)	(0;2 $_{12}$)
1.206	1.882	1.799	1.133	0.823	1.127	1.126	0.823	0.947	1.360	1.353	0.941	0.888	1.299
(0;2 $_{20}$)	(1;2 $_{21}$)	(1;2 $_{11}$)	(1;2 $_{02}$)	(0;2 $_{20}$)	(1;2 $_{21}$)	(1;2 $_{11}$)	(1;2 $_{02}$)	(0;2 $_{20}$)	(1;2 $_{21}$)	(1;2 $_{11}$)	(1;2 $_{02}$)	(0;2 $_{21}$)	(0;2 $_{21}$)
1.799	6.240	6.905	1.882	1.127	8.175	8.445	1.128	1.353	7.260	7.656	1.361	1.321	1.353
(1;2 $_{12}$)	(2;2 $_{11}$)	(2;2 $_{21}$)	(1;2 $_{20}$)	(1;2 $_{12}$)	(2;2 $_{11}$)	(2;2 $_{21}$)	(1;2 $_{20}$)	(1;2 $_{12}$)	(2;2 $_{11}$)	(2;2 $_{21}$)	(1;2 $_{20}$)	(0;2 $_{20}$)	(1;2 $_{02}$)
6.117	10.744	10.095	6.406	8.173	10.163	9.900	8.402	7.233	10.067	9.682	7.470	1.502	1.456
(2;2 $_{02}$)	(3;2 $_{21}$)	(3;2 $_{11}$)	(2;2 $_{12}$)	(2;2 $_{02}$)	(3;2 $_{21}$)	(3;2 $_{11}$)	(2;2 $_{12}$)	(2;2 $_{02}$)	(3;2 $_{21}$)	(3;2 $_{11}$)	(2;2 $_{12}$)	(1;2 $_{12}$)	(1;2 $_{11}$)
$J = 3$													
2.146	1.904	1.829	2.060	1.606	1.477	1.477	1.605	1.815	1.649	1.644	1.808	1.850	1.591
(0;3 $_{22}$)	(0;3 $_{13}$)	(0;3 $_{03}$)	(0;3 $_{12}$)	(0;3 $_{22}$)	(0;3 $_{13}$)	(0;3 $_{03}$)	(0;3 $_{12}$)	(0;3 $_{22}$)	(0;3 $_{13}$)	(0;3 $_{03}$)	(0;3 $_{12}$)	(0;3 $_{31}$)	(0;3 $_{03}$)
2.714	2.042	2.109	2.793	1.866	1.548	1.548	1.867	2.176	1.749	1.754	2.182	2.072	1.640
(1;3 $_{12}$)	(0;3 $_{21}$)	(0;3 $_{31}$)	(0;3 $_{30}$)	(1;3 $_{12}$)	(0;3 $_{21}$)	(0;3 $_{31}$)	(0;3 $_{30}$)	(1;3 $_{12}$)	(0;3 $_{21}$)	(0;3 $_{31}$)	(0;3 $_{30}$)	(0;3 $_{22}$)	(0;3 $_{12}$)
3.901	2.793	2.712	3.815	2.349	1.870	1.869	2.348	2.844	2.185	2.178	2.836	2.175	2.151
(1;3 $_{30}$)	(1;3 $_{13}$)	(1;3 $_{03}$)	(1;3 $_{22}$)	(1;3 $_{30}$)	(1;3 $_{13}$)	(1;3 $_{03}$)	(1;3 $_{22}$)	(1;3 $_{30}$)	(1;3 $_{13}$)	(1;3 $_{03}$)	(1;3 $_{22}$)	(0;3 $_{31}$)	(0;3 $_{21}$)
7.850	3.815	3.901	7.097	9.258	2.348	2.349	8.842	8.533	2.836	2.844	8.013	2.252	2.331
(2;3 $_{22}$)	(1;3 $_{21}$)	(1;3 $_{31}$)	(2;3 $_{12}$)	(2;3 $_{22}$)	(1;3 $_{21}$)	(1;3 $_{31}$)	(2;3 $_{12}$)	(2;3 $_{22}$)	(1;3 $_{21}$)	(1;3 $_{31}$)	(2;3 $_{12}$)	(1;3 $_{03}$)	(0;3 $_{30}$)
$\Delta v_0(V_{\text{MLR}})$		-0.357			-0.258				-0.401			-0.094	
$\Delta v_0(V_{\text{MP4}})^{16}$		-0.44											
$\Delta v_0(\text{obs.})$		-0.401						-0.365					

^aThe assignments in parentheses are ($\nu_i J_{K_a K_c}$).

Rovibrational Energy Levels and Band Origin Shifts.

In Table 2, we report the calculated rovibrational energy levels with $J = 0, 1, 2$, and 3 for $\text{OCS}(\nu_1=0)$ -(hydrogen) $_2$ complexes and for $\text{OCS}(\nu_1=0)$ - $p\text{H}_2$ -He trimer which are relative to the corresponding zero-point levels (-139.718 cm^{-1} for $\text{OCS}-(p\text{H}_2)_2$, -177.057 cm^{-1} for $\text{OCS}-(o\text{D}_2)_2$, -163.895 cm^{-1} for $\text{OCS}-(\text{HD})_2$, and -87.476 cm^{-1} for $\text{OCS}-p\text{H}_2$ -He), respectively. In order to compare with experimental results, quantum numbers ν_i , J , K_a , and K_c are used to label the energy levels, where ν_i is the van der Waals torsional vibration, J is the total angular momentum, and K_a and K_c are the projections of J on the a and c axes. For $\text{OCS}(\text{hydrogen})_2$ complexes, A and B are applied to label the symmetry with respect to permutation of H_2 , and e and f are parity labels. Only levels of (A, e) and (A, f) states are allowed by nuclear spin statistics. For the $\text{OCS}-p\text{H}_2$ -He trimer, even and odd parity blocks are used to clarify the energy levels for lack of exchange symmetry.

The torsional motion state ν_t for $\text{OCS}(\text{hydrogen})_2$ or for $\text{OCS}-p\text{H}_2$ -He is the torsional motion of the two particles around the OCS axis. For $\text{OCS}-(p\text{H}_2)_2$, the excitation energies of $J = 0$ are 0.081, 5.182, 9.023, 14.359, and 20.952 cm^{-1} corresponding to $\nu_t = 1, 2, 3, 4$, and 5 based on the nodal structures along φ coordinate as Figure 6 shown. The level spacing from $\nu_t = 1 \leftarrow 0$ is 0.081 cm^{-1} which is much smaller than the spacing of $\nu_t = 2 \leftarrow 1$ (5.101 cm^{-1}). The small energy gap is readily understood as a tunneling splitting of the symmetric double minimum potential whose barrier maximum linked two $p\text{H}_2$ molecules lying on opposite sides of OCS axis as shown in Figure 4. The tunneling splitting effects decrease in the order of $\text{OCS}-(p\text{H}_2)_2$, $\text{OCS}-(\text{HD})_2$, and $\text{OCS}-(o\text{D}_2)_2$ related to their reduced masses. In contrast, for $\text{OCS}-p\text{H}_2$ -He, the level spacing for $\nu_t = 1 \leftarrow 0$ is very high (0.538 cm^{-1}) relative to the corresponding zero-point level, which indicates the absence of tunneling splitting behavior.

One-dimensional wave functions along the dihedral angle φ are used to assign the torsional motion states ($\nu_t = 0, 1, 2, 3, 4$, and 5) which are obtained by integrating the wave functions over all degrees of freedom as shown in Figure 6. Based on the nodal

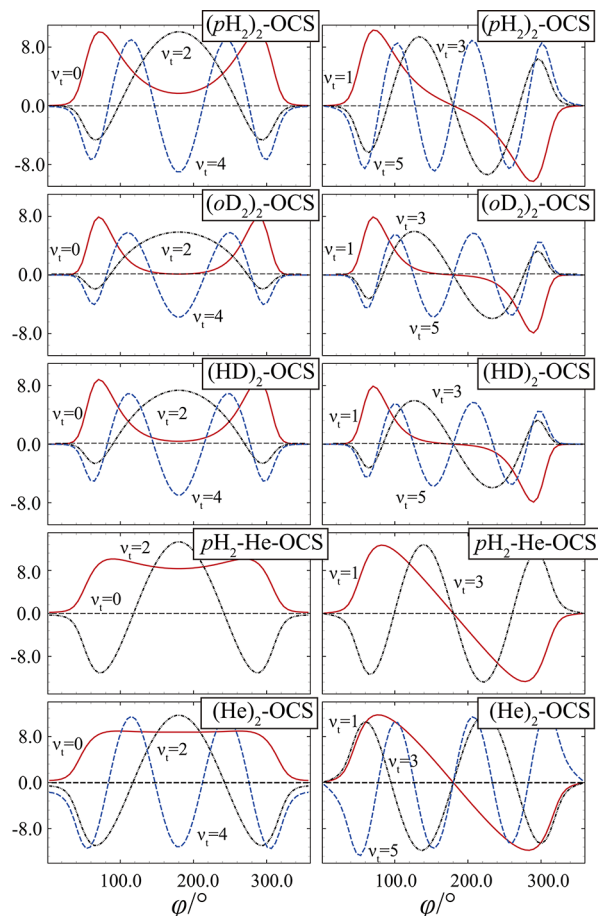


Figure 6. Partial wave functions for the torsional motion ν_t of OCS($\nu_1 = 0$)-(hydrogen)₂ and OCS($\nu_1 = 0$)-pH₂-He complexes as a function of the azimuthal angle φ and compared with OCS($\nu_1 = 0$)-(He)₂ trimer.

structures of the partial wave functions, it is natural to make the assignment for the torsional motion ν_t . The wave functions for OCS-(hydrogen)₂ complexes have strikingly regular nodal structures along the φ coordinate with $\varphi = 0^\circ$ or 180° which indicate the little coupling between φ and the other coordinates. However, for OCS-(He)₂, the wave functions for $\nu_t = 0, 2$, and 4 have no strict nodal structures probably because the strong coupling between φ and the other coordinates disturbs the corresponding characters. It is worth noting that the strong couplings of $\nu_t > 4$ for OCS-pH₂-He make them difficult to assign, so the only lowest four torsional states, therefore, are presented in Figure 6. The wave functions of $\nu_t = 0, 2$, and 4 for OCS-(hydrogen)₂ complexes are similar to each other, while they are much different from those of OCS-pH₂-He and OCS-(He)₂ trimers, especially for $\nu_t = 0$. As shown in Figure 6, the wave functions of $\nu_t = 0$ for OCS-(hydrogen)₂ ($\nu_1 = 0$) complexes are much localized in the global minima regions with $\varphi = 73^\circ$ and 287° . However, for OCS-pH₂-He and OCS-(He)₂ trimers, the wave functions of $\nu_t = 0$ are much more delocalized over the whole space except the excluded volumes near $\varphi = 0^\circ$ and 360° . It is clear to see that the squares of the $\nu_t = 0$ and 1 wave functions are similar to each other for OCS-(hydrogen)₂ complexes, which means the tunneling-splitting behavior is

more likely to appear. For OCS-pH₂-He and OCS-(He)₂ trimers, however, the densities for $\nu_t = 0$ and 1 are quite different from one another, where the tunneling splitting effects are suppressed. Here, the torsion motion levels with odd quantum numbers are not physically permitted for $J = 0$ although ν_t was used here to state the natures of the low energy vibrational modes because pH₂ and He are bosons.

As shown in Table 2, the binding energy for OCS-(pH₂)₂ is 139.718 cm⁻¹ which is 47.46% of the corresponding well depth of 294.407 cm⁻¹. Its well depth is slightly shallower (0.083 cm⁻¹) than the sum of the double well depths of the OCS-pH₂ dimer (134.890 cm⁻¹) plus the depth of the (pH₂)₂ (24.71 cm⁻¹). In addition, the ground state level is 1.697 cm⁻¹ higher than twice of the binding energy of OCS-pH₂²⁸ (67.508 cm⁻¹) plus the binding energy of the (pH₂)₂ dimer. That simple measurement is because the interaction of OCS-(pH₂)₂ neglects the effect of the correlations with the mixing two pH₂ particle wave functions. Similar natures could also be found in OCS-(oD₂)₂, OCS-(HD)₂, and OCS-pH₂-He complexes.

The band origin shifts predicted on our five-dimensional reduced-dimension V_{MLR} PES are obtained by $\Delta\nu_0 = E_{\nu_1=1}^{\text{ZPE}} - E_{\nu_1=0}^{\text{ZPE}}$ which are displayed in Table 3. They are all red shifted with values of -0.3568, -0.2578, and -0.4005 cm⁻¹ for OCS-(pH₂)₂, OCS-(oD₂)₂, and OCS-(HD)₂ trimers, respectively, which are a little more than twice the values of OCS-pH₂, OCS-oD₂, and OCS-HD dimers of -0.172, -0.135, and -0.194 cm⁻¹.²⁸ In addition, the predicted $\Delta\nu_0$ for OCS-pH₂-He is approximately the sum of the band origin shifts of -0.172 (OCS-pH₂) and 0.082 cm⁻¹ (OCS-He).⁴³ The band origin shift for OCS-(pH₂)₂ is 0.044 cm⁻¹ higher than the experimental value of -0.401 cm⁻¹ while the value of V_{MP4} is 0.039 cm⁻¹ lower than the experimental data.¹⁷ For the OCS-(HD)₂ trimer, our predicted band origin shift is 0.036 cm⁻¹ lower than the experimental value.

PREDICTED INFRARED SPECTRA

The rovibrational transition energies are obtained according to

$$\nu = \nu_0 + E_{\nu_t, J, K_a, K_c}^{\nu_t=1} - E_{\nu_t, J, K_a, K_c}^{\nu_t=0} \quad (12)$$

where ν_0 is the C–O stretching vibrational frequency of the free OCS (fixed at the experimental value of 2062.2012 cm⁻¹) and $E_{\nu_t, J, K_a, K_c}^{\nu_t}$ are the rotational energies computed at our 5D V_{MLR} PESs. The calculated infrared transitions relative to the corresponding band origins of OCS with (pH₂)₂, (oD₂)₂, (HD)₂, and OCS-pH₂-He are listed in Table 3 and compared with the available experimental values. According to the selection rules $\Delta J = 0, \pm 1$ and $\Delta P = 1$, there are 400 possible transitions with $J \leq 3$ and $\nu_t \leq 3$. Here, for all cases, we only list the transitions with the intensity greater than 10^{-4} (μ_{CO}^2) at the experiment effective rotational temperature of 0.2 K, and the rest transitions are not listed here because they are too weak to be observed experimentally.

As shown in Table 3, the calculated transitions in columns 2 and 5 agree very well with the observed ones in columns 3 and 6 with root-mean-square deviations (RMSDs) of 0.001 and 0.002 cm⁻¹. The excellent agreement with the experimental values enhances our confidence to assign the unobserved and unidentified transitions for OCS-(pH₂)₂, OCS-(HD)₂, OCS-(oD₂)₂, and OCS-pH₂-He as listed in columns 1, 4, 7, and 8 of Table 3. It is noteworthy that, for the OCS-(pH₂)₂ complex, the observed transition at 2062.695 cm⁻¹ was assigned to be

Table 3. Predicted Infrared Spectra from Vibrationally Averaged Five-Dimensional V_{MLR} PESs for OCS-(Hydrogen)_2 and $\text{OCS-}p\text{H}_2\text{-He}$ Trimers and Compared with the Available Experimental Results

transition	(pH ₂) ₂ -OCS				(HD) ₂ -OCS				(oD ₂) ₂ -OCS				pH ₂ -He-OCS					
	cal.	obs.	diff.	I _{cal.} (0.6K)	I _{cal.} (0.2K)	cal.	obs.	diff.	I _{cal.} (0.6K)	I _{cal.} (0.2K)	cal.	obs.	diff.	I _{cal.} (0.6K)	I _{cal.} (0.2K)	cal.	I _{cal.} (0.6K)	I _{cal.} (0.2K)
band origin	2061.844	2061.800				2061.801	2061.837				2061.943							2062.107
0;1 ₀₁ -0;0 ₀₀	0.304	0.305	0.001	1.000	1.000	0.273	0.272	−0.001	1.000	1.000	0.246	1.000			1.000	0.273	1.000	1.000
0;1 ₁₀ -0;0 ₀₀																0.380	0.086	0.086
1;1 ₁₁ -0;0 ₀₀	0.603			0.027	0.027	0.408			0.080	0.080	0.339	0.190			0.190			
2;1 ₀₁ -0;0 ₀₀	5.495			0.477	0.477	6.683			0.435	0.435	7.693	0.430			0.430	2.908	0.405	0.405
0;1 ₀₁ -0;1 ₁₁																−0.038	0.556	0.075
0;2 ₁₂ -0;1 ₁₁	−0.007			0.163	0.009						−0.010	0.319				0.576	0.512	0.069
1;1 ₁₁ -1;1 ₁₀	8.930			0.146	0.008						9.123	0.321			0.060			
3;1 ₁₁ -1;1 ₁₀	0.610			0.160	0.009						0.500	0.314			0.059			
0;2 ₂₁ -1;1 ₁₀	9.475			0.145	0.008						9.544	0.318			0.060			
3;2 ₁₁ -1;1 ₁₀																		
0;0 ₀₀ -0;1 ₀₁	−0.305	−0.306	−0.001	0.481	0.111	−0.275	−0.273	0.002	0.517	0.139	−0.247	0.552	0.169		0.169	−0.272	0.519	0.140
2;0 ₀₀ -0;1 ₀₁	4.876			0.224	0.052	6.117			0.209	0.056	7.176	0.201			0.061			
0;2 ₀₂ -0;1 ₀₁	0.606	0.606	−0.000	0.878	0.203	0.545	0.543	−0.002	0.808	0.217	0.490	0.653			0.200	0.534	0.742	0.200
0;2 ₁₁ -0;1 ₀₁																0.612	0.264	0.071
0;2 ₂₀ -0;1 ₀₁	0.895	0.897	0.002	0.080	0.019	0.670			0.228	0.061	0.574	0.468			0.143			
2;2 ₀₂ -0;1 ₀₁	5.807			0.433	0.100	6.957			0.378	0.101	7.924	0.317			0.097			
0;1 ₁₁ -0;1 ₁₀																		
0;2 ₁₁ -0;1 ₁₀																		
1;1 ₁₀ -1;1 ₁₁	0.005			0.165	0.009	0.009			0.260	0.036	0.009	0.326			0.064			
3;1 ₁₀ -1;1 ₁₁	8.902			0.145	0.008						9.085	0.280			0.055			
0;2 ₀₂ -1;1 ₁₁											0.397	0.233			0.046			
0;2 ₂₀ -1;1 ₁₁	0.598			0.147	0.008						0.481	0.213			0.042			
0;1 ₀₁ -0;2 ₀₂	−0.611	−0.611	0.000	0.203	0.003													
0;3 ₀₃ -0;2 ₂₀						0.814	0.812	−0.003	0.077	0.001								
RMSE			0.001					0.002										

$0;3_{03}-0;2_{02}$ experimentally. However, according to our prediction, the calculated line position of $0;3_{03}-0;2_{02}$ is 2062.706 cm^{-1} which has a discrepancy of 0.011 cm^{-1} with the experimental value. This discrepancy is almost 1 order of magnitude greater than the rest predictions which makes us prefer to believe that the observed transition (2062.695 cm^{-1}) should be assigned to $0;2_{20}-0;1_{01}$ with a reasonable difference of 0.002 cm^{-1} rather than the nearby transition of $0;3_{03}-0;2_{02}$. The other key point is that the intensity of $0;2_{20}-0;1_{01}$ is 0.018 relative to the strong $0;1_{01}-0;1_{00}$ line which is almost 1 order of magnitude stronger than the relative intensity of 0.003 for $0;3_{03}-0;2_{02}$ at 0.2 K. The overlap of the two transition lines confuses the experimental identification. Therefore, the line located at 2062.695 cm^{-1} should be assigned to $0;2_{20}-0;1_{01}$ which is corrected and bold in Table 3.

Line strengths and intensities of all of the 400 possible transitions subjecting to the selection rules aforementioned at very low experiment effective rotational temperatures (0.2 and 0.6 K) are depicted in Figures 7–10 for OCS-(hydrogen)₂ and

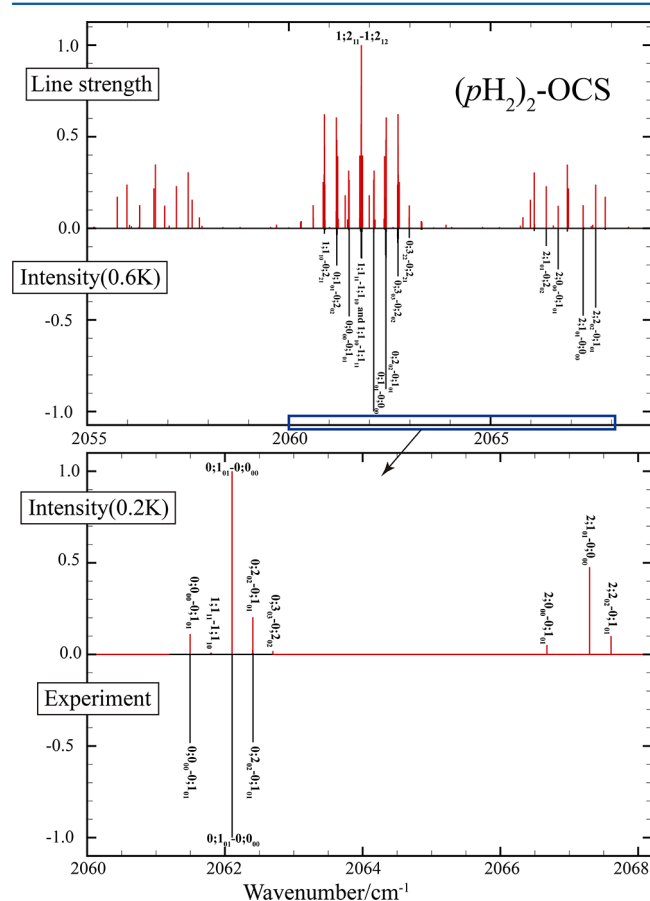


Figure 7. (Upper panel) Calculated infrared spectra of OCS-($p\text{H}_2$)₂ trimer and intensities relative to $0;1_{01}-0;0_{00}$ whose intensity was set to 1.0 at 0.6 K. (Lower panel) Relative intensities at 0.2 K and compared with the available experimental data.

OCS- $p\text{H}_2$ -He trimers. For OCS-($p\text{H}_2$)₂, all of the transitions concentrate at $2055\sim 2058$, $2060\sim 2063$, and $2066\sim 2068\text{ cm}^{-1}$ whose line strengths relative to the strong $1;2_{11}-1;2_{12}$ line are shown in Figure 7. Note that the line strength does not depend on the temperature. The intensities at 0.6 and 0.2 K are all relative to the strong line $0;1_{01}-0;0_{00}$. At 0.6 K, the transitions concentrated at $2060\sim 2063\text{ cm}^{-1}$ mostly belong to $\nu_t = 0 \leftarrow 0$ band. In this region, there is a series of lines that are almost equally spaced marked $0;1_{01}-0;0_{00}$, $0;2_{02}-0;1_{01}$, and $0;3_{03}-0;2_{02}$

($R(0)$, $R(1)$, and $R(2)$). Moving to lower wave numbers, we could find another equally spaced lines assigned $0;0_{00}-0;1_{01}$ and $0;1_{01}-0;2_{02}$ ($P(1)$ and $P(2)$). The only Q-branch we could find is $1;1_{11}-1;1_{10}$ or $1;1_{10}-1;1_{11}$ at 2061.793 or 2061.805 cm^{-1} . The transitions concentrated at $2066\sim 2068\text{ cm}^{-1}$ belong to $\nu_t = 2 \leftarrow 0$ band, and the equally spaced lines are P-branch of $2;1_{01}-0;2_{02}$ and $2;0_{00}-0;1_{01}$ ($P(2)$ and $P(1)$), and R-branch of $2;1_{01}-0;0_{00}$ and $2;2_{02}-0;1_{01}$ ($R(0)$ and $R(1)$). Intensities become weaker with decreasing temperature. This makes the majority of transition lines at 0.2 K unobservable. Thus, the only Q-branch is too weak to be observed experimentally. Comparing with the observed transitions lines ($P(2)$ and $R(2)$ are too weak to be marked in Figure 1 of ref 17), as shown in the lower panel of Figure 7, our predictions are in excellent agreement with the available experimental data in both intensities and transition frequencies. Thus, the weak transition lines that have not been recorded experimentally can only be identified with the present calculations.

Recently, there are two precise microwave transition lines recorded by Raston et al. for OCS-($p\text{H}_2$)₂.⁹ The experimental transitions are 0.307 and 0.613 cm^{-1} for $0;0_{00}-0;1_{01}$ and $0;1_{01}-0;2_{02}$, which are also in good agreement with the present theoretical values of 0.305 and 0.610 cm^{-1} with discrepancies less than 0.003 cm^{-1} .

Compared with OCS-($p\text{H}_2$)₂, similar sequences of transitions can be obtained for OCS-(HD)₂ as depicted in Figure 8.

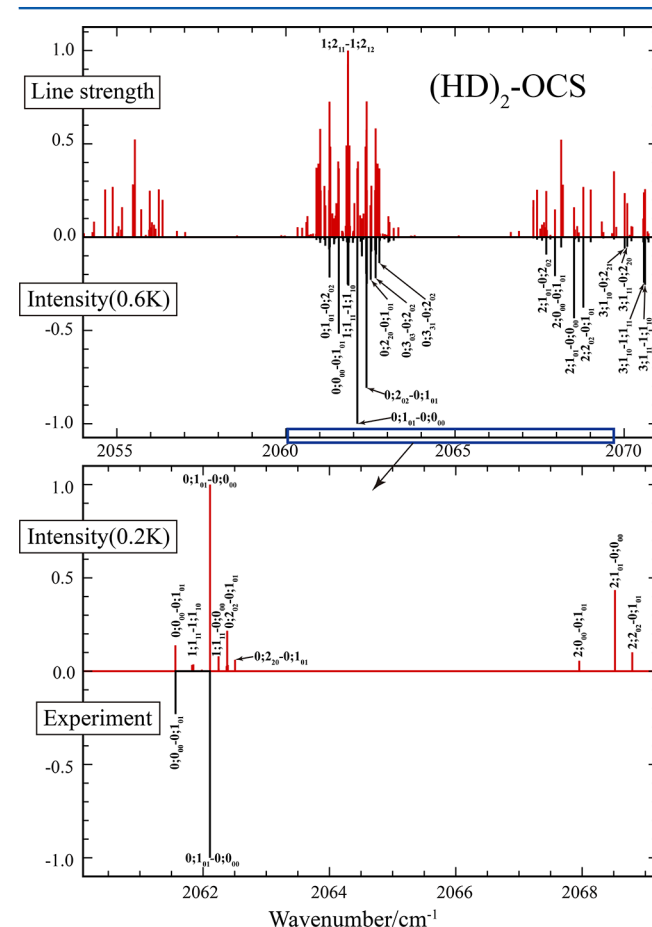


Figure 8. (Upper panel) Calculated infrared spectra of the OCS-(HD)₂ trimer and intensities relative to $1;2_{11}-1;2_{12}$ whose intensity was set to 1.0 at 0.6 K. (Lower panel) Relative intensities at 0.2 K and compared with the available experimental data.

The infrared transitions at 0.6 K concentrate in two regions: one is about 0.3 cm^{-1} red shift from those of $\text{OCS-(pH}_2)_2$ in the $2060\sim 2063 \text{ cm}^{-1}$ region and the other one is about 1.2 cm^{-1} blue shift from those of $\text{OCS-(pH}_2)_2$ in the $2066\sim 2068 \text{ cm}^{-1}$ region. There could also be found equally spaced *P*-branch of $0;0_{00}-0;1_{01}$ and $0;1_{01}-0;2_{02}$ (*P*(1) and *P*(2)) and *R*-branch of $0;1_{01}-0;0_{00}$, $0;2_{02}-0;1_{01}$, and $0;3_{03}-0;2_{02}$ (*R*(0), *R*(1), and *R*(2)). It is more complicated for OCS-(HD)_2 because more transitions could be observed and congested together. For example, there is another *R*(1) ($0;2_{20}-0;1_{01}$) between *R*(1) and *R*(2) ($0;2_{02}-0;1_{01}$ and $0;3_{03}-0;2_{02}$). Furthermore, the intensities of *Q*-branch are so strong that they can be observed at both 0.6 and 0.2 K temperature for OCS-(HD)_2 . Here, we assigned all possible transition lines and compared them with the observed transition lines (*R*(1) and *R*(2) are too weak to be marked in Figure 2 of ref 17). Our predictions are also in good agreement with the observations for the OCS-(HD)_2 complex.

Comparing with $\text{OCS-(pH}_2)_2$ or OCS-(HD)_2 , the transition lines at 0.6 and 0.2 K for $\text{OCS-(oD}_2)_2$ are more crowded with several lines overlap together which makes the assignment even harder as shown in Figure 9. The infrared transitions are more

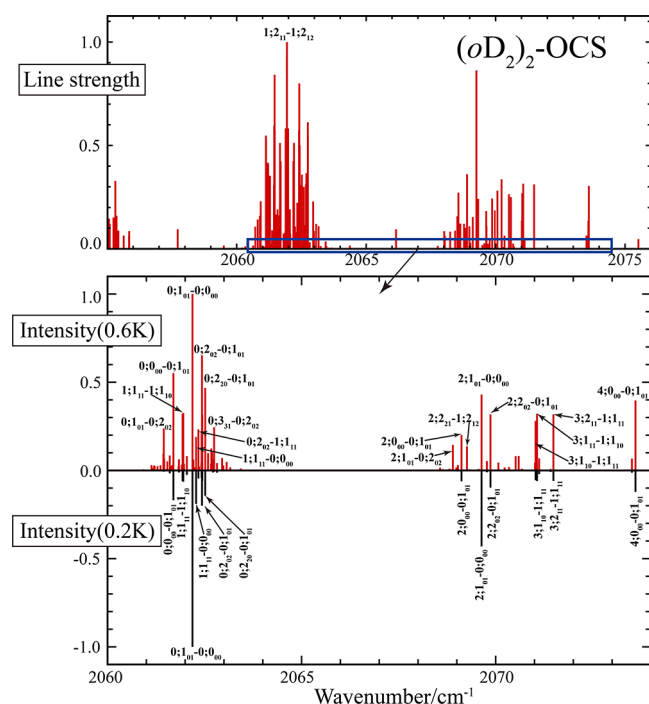


Figure 9. (Upper panel) Calculated infrared spectra of $\text{OCS-(oD}_2)_2$ trimer and line strengths relative to $1;2_{11}-1;2_{12}$. (Lower panel) Intensities relative to $0;1_{01}-0;0_{00}$ whose intensity was set to 1.0 at 0.6 and 0.2 K.

complicated with $\nu_t = 0 \leftarrow 0$, $\nu_t = 0 \leftarrow 1$, $\nu_t = 1 \leftarrow 0$, and $\nu_t = 1 \leftarrow 1$ concentrating at $2061\sim 2063 \text{ cm}^{-1}$ and with $\nu_t = 2 \leftarrow 0$ and $\nu_t = 4 \leftarrow 0$ concentrating at the $2069\sim 2074 \text{ cm}^{-1}$ region. There are several *Q*-branches that could be found (e.g., $1;1_{11}-1;1_{10}$, $3;1_{10}-1;1_{11}$, and $3;1_{11}-1;1_{10}$) for $\text{OCS-(oD}_2)_2$ due to their strong intensities for both temperatures. The crowd cases are more serious for the $\text{OCS-pH}_2\text{-He}$ complex as depicted in Figure 10. The infrared transitions almost spread in the $2061\sim 2065 \text{ cm}^{-1}$ region. The *Q*-branch, as expected, is present for both temperatures ($0;1_{10}-0;1_{11}$ and $0;1_{11}-0;1_{10}$). Their detailed assignments will become possible with the help of the present theoretical calculations.

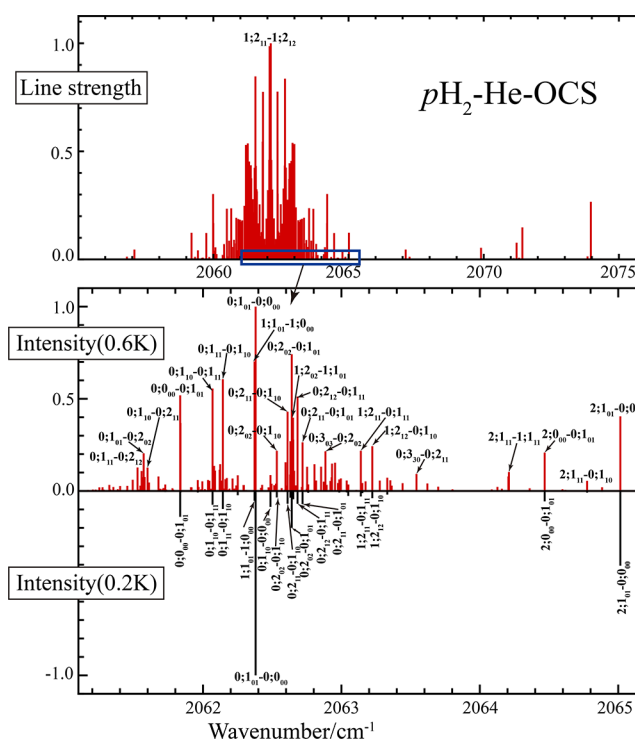


Figure 10. (Upper panel) Calculated infrared spectra of $\text{OCS-pH}_2\text{-He}$ trimer and line strengths relative to $0;2_{20}-0;2_{21}$. (Lower panel) Intensities relative to $0;1_{01}-0;0_{00}$ whose intensity was set to 1.0 at 0.6 and 0.2 K.

“SOLVENT” DENSITY DISTRIBUTIONS OF pH_2 OR He AROUND OCS

Figure 11 presents the density distributions of the two pH_2 , two He atoms, or the mixed of pH_2 and He in the body-fixed frame

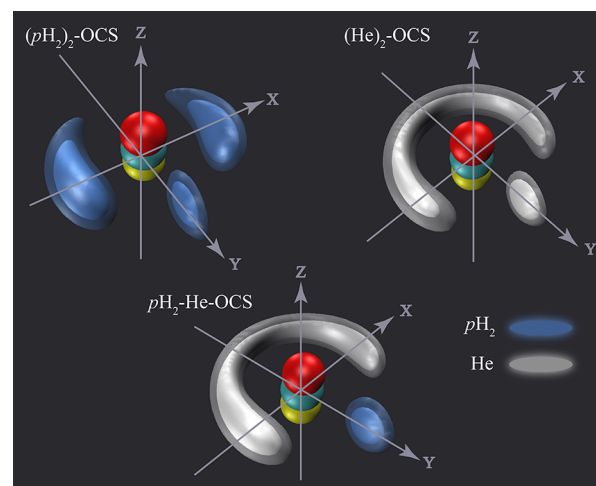


Figure 11. Three dimensional density distribution of pH_2 for the $\text{OCS}(\nu_1 = 0)\text{-(pH}_2)_2$ trimer in the body-fixed frame and compared with the density distributions of $\text{pH}_2\text{-He}$ and He around $\text{OCS}(\nu_1 = 0)\text{-pH}_2\text{-He}$ and $\text{OCS}(\nu_1 = 0)\text{-(He)}_2$. The first pH_2 or He locates at the *yz* plane, while the density of pH_2 or He from the second one is on the *xy* plane because the density was obtained with the values of Gaussian standard deviations defining the densities at $\sigma_x = \sigma_y = 0.25 \text{ \AA}$ and $\sigma_z = 0.1 \text{ \AA}$ for particle 1 and at $\sigma_x = \sigma_y = \sigma_z = 0.25 \text{ \AA}$ for particle 2.

for the ground states of $\text{OCS-(pH}_2)_2$, $\text{OCS-pH}_2\text{-He}$, or OCS-(He)_2 trimers with the procedure described in ref 39. As seen in Figure 11, the OCS molecular is placed at the *z* axis in the

density iso-surfaces. In addition, the densities of the first $p\text{H}_2$ or He distribute in the yz plane like a thin slice while the second one spreads over the xy plane. The significant difference between the two particles (two $p\text{H}_2$, $p\text{H}_2$ and He atom, or two He atoms) attributes to that the position of the first $p\text{H}_2$ or He atom was defined as yz plane of the body-fixed frame, and hence its density naturally distributes with respect to the y direction. The reason why the first particle's density distribution is not zero in the y direction is the use of a finite bin size ($\sigma_y > 0$) in the calculation. For the $\text{OCS-(}p\text{H}_2)_2$ trimer, the density distribution of the second $p\text{H}_2$ is highly localized with the regions associated with the $p\text{H}_2$ - $p\text{H}_2$ potential minimum as seen in Figure 11. However, the pronounced location is missing in $\text{OCS-}p\text{H}_2$ -He or OCS-(He)_2 trimer with even forming more than a half circle around OCS. That stems from the weak OCS-He and He-He interactions. In addition, comparing $\text{OCS-}p\text{H}_2$ -He with OCS-(He)_2 , the second He atoms have a thin density between the two minima for $\text{OCS-}p\text{H}_2$ -He while they have a uniform distribution for OCS-(He)_2 trimer due to the stronger interaction of $p\text{H}_2$ -He. For all of the cases, the large gap between the first $p\text{H}_2$ or He and the second particle is derived from the short-range repulsive wall of the $p\text{H}_2$ - $p\text{H}_2$, $p\text{H}_2$ -He, or He-He potentials.

The "solvent" of $p\text{H}_2$, $p\text{H}_2$ -He, and He-He in the first three torsional levels is depicted in Figure 12 for $\text{OCS-(}p\text{H}_2)_2$,

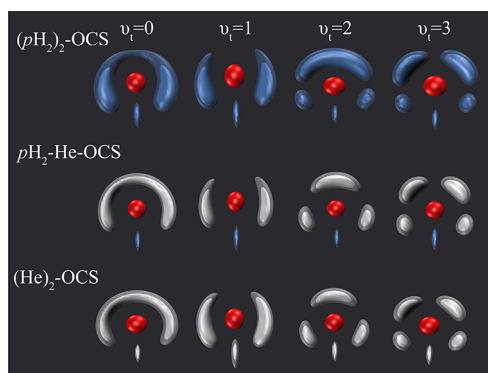


Figure 12. Three-dimensional density distributions for $\text{OCS-(}p\text{H}_2)_2$, $\text{OCS-}p\text{H}_2$ -He, and OCS-(He)_2 trimers in their four lowest torsion vibrational levels.

$\text{OCS-}p\text{H}_2$ -He, and OCS-(He)_2 trimers, respectively. As shown in Figure 12, for all of the cases, the density distributions for $v_t = 0$ are much different, while they are almost the same for $v_t = 1, 2$, and 3 which are consistent with the nodal structures shown in Figure 6.

CONCLUSIONS

Calculated rovibrational energy levels and predicted infrared spectra for OCS-(hydrogen)_2 and $\text{OCS-}p\text{H}_2$ -He are obtained and assigned from the global potential energy surface defined as a sum of OCS-hydrogen and hydrogen-hydrogen or $p\text{H}_2$ -He pair potentials. It should be noted that the three-body contributions to the interactions are neglected here. The calculated band origin shifts (-0.357 cm^{-1} for $\text{OCS-(}p\text{H}_2)_2$ and -0.401 cm^{-1} for OCS-(HD)_2) are in good agreement with the available experimental data (-0.40 cm^{-1} for $\text{OCS-(}p\text{H}_2)_2$ and for OCS-(HD)_2 -0.365 cm^{-1}). Moreover, the predicted infrared spectra for $\text{OCS-(}p\text{H}_2)_2$ are in excellent accordance with the observed values in both positions and intensities at the effective rotational temperature of 0.2 K , which validate the reduced dimensional treatment of AHR method and the ignorance

of the three-body potential. Based on the high-quality PESs, we reassigned the infrared transition (in one case) and extended the assignments to the unrecorded transition lines for $\text{OCS-(}p\text{H}_2)_2$ and for OCS-(HD)_2 . Simultaneously, for the more complicated complexes, the infrared spectra of $\text{OCS-(oD}_2)_2$ and $\text{OCS-}p\text{H}_2$ -He are assigned for the first time.

The three-dimensional density distributions of the second hydrogen or helium relative to the positions of the first one are shown in Figures 11 and 12 using the visualizing method. For the ground state of the $\text{OCS-(}p\text{H}_2)_2$ complex, the $p\text{H}_2$ is much localized in the region of the global minimum. In contrast, the He in $\text{OCS-}p\text{H}_2$ -He or OCS-(He)_2 is highly delocalized with forming an uncompleted circle around the OCS axis. For all of the cases, the excluded densities between particle 1 and particle 2 are due to the $p\text{H}_2$ - $p\text{H}_2$, He-He , or $p\text{H}_2$ -He repulsions.

ASSOCIATED CONTENT

Supporting Information

The Supporting Information is available free of charge on the ACS Publications website at DOI: 10.1021/acs.jpca.7b12708.

Table S1 presents the calculated rovibrational energy levels (in cm^{-1}) with $J = 0, 1, 2$, and 3 for $\text{OCS}(v_1 = 1)$ -(hydrogen) $_2$ complexes and for the $\text{OCS}(v_1 = 1)$ - $p\text{H}_2$ -He trimer which are relative to the corresponding zero-point levels. (PDF)

AUTHOR INFORMATION

Corresponding Author

*E-mail: prof_huili@jlu.edu.cn

ORCID

Hui Li: 0000-0002-2689-2241

Notes

The authors declare no competing financial interest.

ACKNOWLEDGMENTS

The authors thank the National Natural Science Foundation of China (Grant Nos. 21773081, 21533003, and 91541124) and National Key Research and Development Program (Nos. 2017YFB0203401 and 2016YFB0700801) for the support.

REFERENCES

- (1) Li, H.; Le Roy, R. J.; Roy, P.-N.; McKellar, A. Molecular superfluid: nonclassical rotations in doped para-hydrogen cluster. *Phys. Rev. Lett.* **2010**, *105*, 133401.
- (2) Ran, H.; Zhou, Y.; Xie, D. Five-dimensional ab initio potential energy surface and predicted infrared spectra of H_2 - CO_2 van der Waals complexes. *J. Chem. Phys.* **2007**, *126*, 204304.
- (3) Jankowski, P.; Surin, L. A.; Potapov, A.; Schlemmer, S.; McKellar, A. R. W.; Szalewicz, K. A comprehensive experimental and theoretical study of H_2 - CO spectra. *J. Chem. Phys.* **2013**, *138*, 084307.
- (4) Zeng, T.; Roy, P.-N. Microscopic molecular superfluid response: theory and simulations. *Rep. Prog. Phys.* **2014**, *77*, 046601.
- (5) Raston, P.; Jäger, W.; Li, H.; Le Roy, R.; Roy, P.-N. Persistent molecular superfluid response in doped para-hydrogen clusters. *Phys. Rev. Lett.* **2012**, *108*, 253402.
- (6) Yoshioka, K.; Anderson, D. T. Infrared spectra of $\text{CH}_3\text{F(ortho-} \text{H}_2)_n$ clusters in solid parahydrogen. *J. Chem. Phys.* **2003**, *119*, 4731–4742.
- (7) Tang, J.; McKellar, A. Infrared spectra of seeded hydrogen clusters: $(\text{para-} \text{H}_2)_N\text{-N}_2\text{O}$ and $(\text{ortho-} \text{H}_2)_N\text{-N}_2\text{O}$, $N = 2\text{--}13$. *J. Chem. Phys.* **2005**, *123*, 114314.

- (8) Li, H.; Roy, P.-N.; Le Roy, R. J. Analytic Morse/long-range potential energy surfaces and predicted infrared spectra for $\text{CO}_2\text{--H}_2$. *J. Chem. Phys.* **2010**, *132*, 214309.
- (9) Raston, P. L.; Jäger, W. Rotational Spectroscopic Study of Quantum Solvation in Isotopologic $(\text{pH}_2)_N\text{--CO}$ Clusters. *J. Phys. Chem. A* **2017**, *121*, 3671–3678.
- (10) Grebenev, S.; Sartakov, B.; Toennies, J. P.; Vilesov, A. F. Evidence for superfluidity in para-hydrogen clusters inside helium-4 droplets at 0.15 kelvin. *Science* **2000**, *289*, 1532–1535.
- (11) Grebenev, S.; Sartakov, B.; Toennies, J. P.; Vilesov, A. Effect of the Symmetry of H_2 Molecules on their Rotations around an OCS Molecule in Superfluid ^4He Droplets. *Phys. Rev. Lett.* **2002**, *89*, 225301.
- (12) Grebenev, S.; Lugovoi, E.; Sartakov, B. G.; Toennies, J. P.; Vilesov, A. F. Spectroscopy of OCS-hydrogen clusters in He droplets. *Faraday Discuss.* **2001**, *118*, 19–32.
- (13) Grebenev, S.; Sartakov, B.; Toennies, J.; Vilesov, A. Infrared Q-branch anomalies on cooling small $\text{OCS}(\text{pH}_2)_n$ clusters from 0.38 to 0.15 K. *Europhys. Lett.* **2008**, *83*, 66008.
- (14) Grebenev, S.; Sartakov, B. G.; Toennies, J. P.; Vilesov, A. F. Spectroscopic investigation of OCS $(\text{p-H}_2)_n$ ($n = 1\text{--}16$) complexes inside helium droplets: Evidence for superfluid behavior. *J. Chem. Phys.* **2010**, *132*, 064501.
- (15) Tang, J.; McKellar, A. Infrared spectra of OCS-hydrogen complexes. *J. Chem. Phys.* **2002**, *116*, 646–653.
- (16) Paesani, F.; Whaley, K. Potential energy surface and infrared spectra of OCS-hydrogen complexes. *Mol. Phys.* **2006**, *104*, 61–72.
- (17) Tang, J.; McKellar, A. Infrared spectra of seeded hydrogen clusters: $(\text{para-H}_2)_N\text{--OCS}$, $(\text{ortho-H}_2)_N\text{--OCS}$, and $(\text{HD})_N\text{--OCS}$, $N = 2\text{--}7$. *J. Chem. Phys.* **2004**, *121*, 3087–3095.
- (18) Yu, Z.; Higgins, K. J.; Klemperer, W.; McCarthy, M. C.; Thaddeus, P. Nuclear hyperfine interaction of rotating hydrogen: A spectroscopic investigation of hydrogen-OCS van der Waals complexes. *J. Chem. Phys.* **2005**, *123*, 221106.
- (19) Yu, Z.; Higgins, K. J.; Klemperer, W.; McCarthy, M. C.; Thaddeus, P.; Liao, K.; Jäger, W. Rotational spectra of the van der Waals complexes of molecular hydrogen and OCS. *J. Chem. Phys.* **2007**, *127*, 054305.
- (20) Michaud, J. M.; Jäger, W. Rotational spectroscopic study of carbonyl sulfide solvated with hydrogen molecules. *J. Chem. Phys.* **2008**, *129*, 144311.
- (21) Michaud, J. M.; Liao, K.; Jäger, W. High-resolution rotational spectroscopy of $\text{H}_2\text{--OCS}$: a study of minor isotopomers of OCS. *Mol. Phys.* **2008**, *106*, 23–31.
- (22) Raston, P. L.; Knapp, C. J.; Jäger, W. Microwave spectroscopy of carbonyl sulfide isotopologues solvated with 2–5 para-hydrogen molecules. *J. Mol. Spectrosc.* **2017**, *341*, 23.
- (23) Kwon, Y.; Whaley, K. B. Nanoscale molecular superfluidity of hydrogen. *Phys. Rev. Lett.* **2002**, *89*, 273401.
- (24) Piccarreta, C.; Gianturco, F. The structuring of a molecular dopant in a quantum solvent. *Eur. Phys. J. D* **2006**, *37*, 93–103.
- (25) Paesani, F.; Zillich, R.; Whaley, K. OCS in small para-hydrogen clusters: Energetics and structure with $N = 1\text{--}8$ complexed hydrogen molecules. *J. Chem. Phys.* **2003**, *119*, 11682.
- (26) Paesani, F.; Zillich, R.; Kwon, Y.; Whaley, K. OCS in para-hydrogen clusters: Rotational dynamics and superfluidity. *J. Chem. Phys.* **2005**, *122*, 181106.
- (27) Paesani, F.; Whaley, K. B. Vibrational shifts of OCS in mixed clusters of parahydrogen and helium. *J. Chem. Phys.* **2006**, *124*, 234310.
- (28) Liu, J.-M.; Zhai, Y.; Li, H. Explicit correlation treatment of the six-dimensional potential energy surface and predicted infrared spectra for OCS--H_2 . *J. Chem. Phys.* **2017**, *147*, 044313.
- (29) Li, H.; Roy, P.-N.; Le Roy, R. J. An "adiabatic-hindered-rotor" treatment allows para- H_2 to be treated as if it were spherical. *J. Chem. Phys.* **2010**, *133*, 104305.
- (30) Li, H.; McKellar, A.; Le Roy, R. J.; Roy, P.-N. Theoretical and Experimental Study of Weakly Bound $\text{CO}_2\text{--}(\text{pH}_2)_2$ Trimers. *J. Phys. Chem. A* **2011**, *115*, 7327–7337.
- (31) Zhang, X.-L.; Li, H.; Le Roy, R. J.; Roy, P.-N. Microwave and infrared spectra of $\text{CO--}(\text{pH}_2)_2$, $\text{CO--}(\text{oD}_2)_2$, and mixed $\text{CO--pH}_2\text{--He}$ trimers. *Theor. Chem. Acc.* **2014**, *133*, 1568.
- (32) Wang, L.; Xie, D.; Le Roy, R. J.; Roy, P.-N. A new six-dimensional potential energy surface for $\text{H}_2\text{--N}_2\text{O}$ and its adiabatic-hindered-rotor treatment. *J. Chem. Phys.* **2013**, *139*, 034312.
- (33) Zeng, T.; Li, H.; Roy, P.-N. Simulating asymmetric top impurities in superfluid clusters: a para-water dopant in para-hydrogen. *J. Phys. Chem. Lett.* **2013**, *4*, 18–22.
- (34) Ziemkiewicz, M. P.; Pluetzer, C.; Nesbitt, D. J.; Scribano, Y.; Faure, A.; Van Der Avoird, A. Overtone vibrational spectroscopy in $\text{H}_2\text{--H}_2\text{O}$ complexes: A combined high level theoretical ab initio, dynamical and experimental study. *J. Chem. Phys.* **2012**, *137*, 084301.
- (35) Wang, X.-G.; Carrington, T., Jr; Tang, J.; McKellar, A. Theoretical and experimental studies of the infrared rovibrational spectrum of $\text{He}_2\text{--N}_2\text{O}$. *J. Chem. Phys.* **2005**, *123*, 034301.
- (36) Mladenović, M. Rovibrational Hamiltonians for general polyatomic molecules in spherical polar parametrization. I. Orthogonal representations. *J. Chem. Phys.* **2000**, *112*, 1070–1081.
- (37) Wang, X.-G.; Carrington, T., Jr; McKellar, A. Theoretical and Experimental Study of the Rovibrational Spectrum of $\text{He}_2\text{--CO}$. *J. Phys. Chem. A* **2009**, *113*, 13331–13341.
- (38) Tang, J.; McKellar, A.; Wang, X.-G.; Carrington, T. Theoretical and experimental study of infrared spectra of $\text{He}_2\text{--CO}_2$. *Can. J. Phys.* **2009**, *87*, 417–423.
- (39) Li, H.; Liu, Y.; Jäger, W.; Le Roy, R. J.; Roy, P.-N. Theoretical study of the microwave spectrum of isotopologues of $\text{OCS--}(\text{He})_2$. *Can. J. Chem.* **2010**, *88*, 1146–1154.
- (40) Gatti, F.; et al. Vector parametrization of the N-atom problem in quantum mechanics. I. Jacobi vectors. *J. Chem. Phys.* **1998**, *108*, 8804–8820.
- (41) Yu, H.-G. Accelerating the calculation of the rovibrational energies of tetraatomic molecules using a two-layer Lanczos algorithm. *Chem. Phys. Lett.* **2002**, *365*, 189–196.
- (42) Patkowski, K.; Cencek, W.; Jankowski, P.; Szalewicz, K.; Mehl, J. B.; Garberoglio, G.; Harvey, A. H. Potential energy surface for interactions between two hydrogen molecules. *J. Chem. Phys.* **2008**, *129*, 094304.
- (43) Li, H.; Ma, Y.-T. An intramolecular vibrationally excited intermolecular potential for He--OCS : Globally tested by simulation of vibrational shifts for OCS in He_N , $N = 1\text{--}100$ Clusters. *J. Chem. Phys.* **2012**, *137*, 234310.
- (44) Light, J.; Hamilton, I.; Lill, J. Generalized discrete variable approximation in quantum mechanics. *J. Chem. Phys.* **1985**, *82*, 1400–1409.
- (45) Colbert, D. T.; Miller, W. H. A novel discrete variable representation for quantum mechanical reactive scattering via the S-matrix Kohn method. *J. Chem. Phys.* **1992**, *96*, 1982–1991.
- (46) Chen, R.; Guo, H. A single Lanczos propagation method for calculating transition amplitudes. II. Modified QL and symmetry adaptation. *J. Chem. Phys.* **2001**, *114*, 1467–1472.
- (47) Wang, X.-G.; Carrington, T., Jr. A symmetry-adapted Lanczos method for calculating energy levels with different symmetries from a single set of iterations. *J. Chem. Phys.* **2001**, *114*, 1473–1477.
- (48) Saupe, S.; Wappelhorst, M. H.; Meyer, B.; Urban, W.; Maki, A. G. Sub-Doppler heterodyne frequency measurements near $5\text{ }\mu\text{m}$ with a CO-laser sideband system: improved calibration tables for carbonyl sulfide transitions. *J. Mol. Spectrosc.* **1996**, *175*, 190–197.
- (49) Bramley, M. J.; Tromp, J. W.; Carrington, T., Jr; Corey, G. C. Efficient calculation of highly excited vibrational energy levels of floppy molecules: The band origins of H_3^+ up to $35\text{ }000\text{ cm}^{-1}$. *J. Chem. Phys.* **1994**, *100*, 6175–6194.
- (50) Bishop, D. M.; Cheung, L. M. Dynamic dipole polarizability of H_2 and HeH^+ . *J. Chem. Phys.* **1980**, *72*, 5125–5132.
- (51) Parker, G. A.; Snow, R. L.; Pack, R. T. Intermolecular potential surfaces from electron gas methods. I. Angle and distance dependence of the He--CO_2 and Ar--CO_2 interactions. *J. Chem. Phys.* **1976**, *64*, 1668–1678.

(52) Kumar, A.; Meath, W. J. Dipole oscillator strength distributions and properties for SO₂, CS₂, and OCS. *Can. J. Phys.* **1985**, *63*, 417–427.

(53) Olney, T. N.; Cann, N.; Cooper, G.; Brion, C. Absolute scale determination for photoabsorption spectra and the calculation of molecular properties using dipole sum-rules. *Chem. Phys.* **1997**, *223*, 59–98.